PCCP

Accepted Manuscript

ROYAL SOCIETY OF CHEMISTRY

www.rsc.org/pccp

PCCP Physical Chemistry Chemical Physics Dynamic Article Links ►

Cite this: DOI: 10.1039/c0xx00000x

www.rsc.org/xxxxxx

ARTICLE TYPE

Incorporation of Zn^{2+} ions into $BaTiO_3$:Er^{3+}/Yb^{3+} nanophosphor: an effective way to enhance upconversion, defect luminescence and temperature sensing

Manoj Kumar Mahata[*a,b], Tristan Koppe[a], Tanusree Mondal[b], Christoph Brüsewitz[a], Kaushal Kumar[b], Vineet Kr. Rai[b], Hans Hofsäss[a], Ulrich Vetter[a]

Received (in XXX, XXX) Xth XXXXXXXXX 20XX, Accepted Xth XXXXXXXXX 20XX
DOI: 10.1039/b000000x

The ferroelectric $BaTiO_3$ has been turned into a multifunctional material via doping of lanthanide ions (0.3 mol% Er^{3+} / 3.0 mol% Yb^{3+}) and subsequently upconversion luminescence was enhanced by incorporation of Zn^{2+} ions. Upconversion luminescence of $BaTiO_3$: Er^{3+}/Yb^{3+} perovskite nanophosphor has been studied using 800 and 980 nm laser excitations. The emission dynamics is studied with respect to its dependence on input power and external temperature including lifetime. Based on time-resolved spectroscopy, it is inferred that two types of Er^{3+} sites are present in the barium titanate lattice. The first one is short lived component (minor species) present at 6-coordinated Ti-sites of low symmetry while the second one is a long lived component (major species), present at 12-coordinated Ba-sites with high symmetry. The influence of the introduction of Zn^{2+} ions on the lifetime of $^4S_{3/2}$ and $^4F_{9/2}$ levels of Er^{3+} ions is also investigated. Enhanced temperature sensing performance (120K to 505K) of the material is observed using the fluorescence intensity ratio technique, employing the emission from the thermally coupled, $^2H_{11/2}$ and $^4S_{3/2}$ energy levels of Er^{3+} ions. The defect luminescence of the material is also found to increase on Zn-doping.

1. Introduction

Rare earth doped phosphor materials are extensively investigated because of their wide field of attractive applications from solid state lighting, display devices, fiber-optic communication, LEDs. to biomedical and therapeutic applications [1-6]. With the prevalent developments in nanotechnology and chemical synthesis processes, a striking interest is noticed to achieve control over the morphology and structures of the phosphor materials in order to optimize the luminescence emission efficiency with respect to specific technological requirements [7]. Furthermore, the public need of cheap and reliable multitasking materials also motivated researchers to think on multifunctional and hybrid materials.

It is known to us that the rare earth ions (RE) show luminescence not only of Stokes type (downconversion) but also of anti-Stokes type (upconversion) and the superiority of the latter one is already well established [8]. Upconversion luminescence is found to be strong in low phonon frequency hosts and out of oxide and halide compounds, oxides have been marked as efficient matrices for lanthanide doping because of their superior chemical stability and durability. Barium titanate is a promising perovskite ferroelectric material which is employed as multilayer capacitor, positive co-efficient resistor, piezoelectric transducer, optical memory etc. [9-11]. The minute incorporation of RE ions in barium titanate can extend its functionality towards phosphor based applications including field emission displays, light emitting devices, remote temperature sensors, and security purposes. Moreover, doping of RE ions in $BaTiO_3$ has proven to be effective for the tuning of dielectric and optical properties [12, 13]. The structural information of this material can also be easily obtained by monitoring the luminescence through doping of small quantity of RE ions [14]. Certain rare earth ions such as Er^{3+}, Yb^{3+}, Dy^{3+}, Ho^{3+} can enhance the electrochemical properties of barium titanate [15]. It is supposed that small sized RE^{3+} ions occupy the Ti-site creating an additional oxygen vacancy (V_O), midsized RE^{3+} ions substitute Ba and Ti site via self-compensation and large RE^{3+} occupy Ba-sites creating a titanium vacancy (V_{Ti}). A substitution mechanism of RE ions depending on ionic radii through a series of classical force field simulations has been inferred by *Dawson et al.* [16]. *Zhang et al.* [17] have studied Er^{3+} substitutions at Ba and Ti sites in $BaTiO_3$ with temperature dependence of the upconversion emission for the identification of structural phase transition.

The upconverting nanoparticles, however, are suffering from low quantum emission efficiency. Therefore, several methods have been employed to improve the luminescence intensity in an internal as well as in an external way, such as formation of core/shell structure, crystal surface coating, varying crystal phases, co-doping with sensitizers etc. [18]. These trials have

their limitations and maximum upconversion efficiency reported till date is below 20% and to increase the upconversion efficiency is still a tough challenge.

The role of transition metal dopants in controlling the properties of $BaTiO_3$ is of fundamental as well as technological interest. Some past reports have provided a catalogue of the possible transition metals which can be stabilized in $BaTiO_3$ [19]. Due to the small ionic radius, Zn^{2+} is favourable for its movement and localization in the barium titanate lattice. The Zn^{2+} can occupy substitutional as well as interstitial sites in the $BaTiO_3$ lattice and breaks the crystal field symmetry around the RE ions. Some works have been done to observe the effect of Zn-doping on the microstructure and dielectric properties of $BaTiO_3$ with a conclusion that Zn-addition to $BaTiO_3$ has several advantages such as decrease in the loss tangent value, formation of heterogeneous microstructures through exaggerated grain growth and generation of second phase because of inhomogeneous processing, improvement in temperature dependence of dielectric constant etc. [20-23]. So, in a word, Zn-addition improves the microstructure and dielectric properties of barium titanate.

During the operation of electronic and photonic devices, temperature is needed to be monitored for the best performance [24]. Therefore, accurate sensing and mapping of temperature in a non-invasive way is a challenging field of research. Hence, this research-need also motivated us to tailor the structural and optical properties of $BaTiO_3$: Er^{3+}/Yb^{3+} nanocrystals with Zn^{2+} ions incorporation and to study the temperature sensing performance. This study explains time-resolved spectroscopy in view of the site substitution of Er^{3+} ions in barium titanate lattice. This work concludes that doping of Zn^{2+} with Er^{3+}/Yb^{3+} ions is a promising route to enhance the multi-functionality of $BaTiO_3$.

2. Experimental

2.1 Material synthesis

The wet-chemical co-precipitation route was followed to synthesize the material. The composition of the sample was as follows:

(100-x-y-z) mol% $BaTiO_3$ + x mol% Er_2O_3 + y mol% Yb_2O_3 + z mol% ZnO

where, x= 0.3, y= 3.0 and z= 0, 10, 20.

The optimized concentration for Er^{3+} and Yb^{3+} was 0.3 and 3mol% respectively [25-27]. In a typical synthesis procedure, provided in our previous report [28], barium carbonate (GR 99%; Merck, India), acetic acid (Glacial 99.9%; Otto, India), titanium tetra-isopropoxide (97%; Otto, India), ytterbium acetate (99.9%; Otto, India), erbium acetate (99.9%; Otto, India) and zinc acetate (GR 99%; Otto, India) were taken as starting precursors. The 1.4 gm of barium carbonate as per above composition was dissolved in 1 ml of acetic acid, warmed for complete dissolution and then cooled down to room temperature. The desired amounts of erbium acetate (0.3 mol%), ytterbium acetate (3.0 mol%) and zinc acetate (0, 10, 20 mol%) were mixed with this solution. Titanium tetra-isopropoxide ($C_{12}H_{28}O_4Ti$) of 1.8 ml were added to the solution and stirred for 1 h. Finally, 10 ml of distilled water were added to the solution for precipitation. The precipitated was collected and washed 5-6 times with de-ionized water and ethanol. After washing, powder samples were dried at room temperature for 24 hours and then annealed at 850 ^{0}C for two hours in a muffle furnace.

2.2 Material characterization

X-ray diffraction measurements were performed on Bruker D8 Advance X-ray diffractometer using Cu-Kα (1.5405 Å) radiation. Infrared absorption spectra were recorded on FTIR spectrometer (Perkin Elmer, Spectrum RX I) using KBr pellet technique with a resolution of 4 cm^{-1}. Scanning electron microscopy (SEM) images were taken on Leo SUPRA 35. For the transmission electron microscopy (TEM), the powder sample was dispersed in ethanol and dropped onto porous carbon film supported on copper grids, and then dried in vacuum. Philips CM 120 transmission electron microscope was used to record the TEM images. The UV-Visible-NIR absorption spectra were taken in diffuse reflectance mode on Lambda 950, UV-VIS-NIR spectrophotometer (Perkin Elmer). The upconversion emission spectra were recorded using 800 and 980 nm laser excitations. The upconversion (UC) emission spectra using 980 nm diode laser were recorded on SP2300 grating spectrometer (Princeton Instruments, USA). Temperature dependent emission studies from 300K to 505K were performed by placing the samples in a homemade oven and temperature was measured with the help of a thermocouple located close (~2 mm) to the laser focus spot on the sample. The temperature dependent UC emissions from 120K to 300K were measured on SPEX 1000M spectrometer. The sample chamber was cooled down by using a He-closed-cycle refrigerator at 10^{-7} mbar pressure. The lifetime measurements were carried out under excitation of 800 nm light emitted from a Ti-sapphire laser, Mira 900-F (Coherent) pumped by 532nm laser (Verdi 10) with fluorescence set up consisting of a streak camera (Hamamatsu C10910), water-cooled CCD (Hamamatsu Orca R2), a synchronous delay generator (Hamamatsu C10647-01), a delay unit (Hamamatsu C1097-05) and a chopper wheel at 250 Hz frequency was used to produce slow laser 'pulses'. The cathodoluminescence measurements were performed at 12K on SPEX 1000M spectrometer at 5 keV accelerating voltage and 1.08 μA emission current under 10^{-7} mbar pressure.

3. Results and discussion

3.1 Structural properties

3.1.1 X-ray diffraction analysis

The XRD patterns of three $BaTiO_3$ samples are shown in Fig. 1. All the detectable peaks have been indexed to cubic-$BaTiO_3$ found in the standard reference (ICDD card no. 75-0461) and no extra peak is found for other phases. Barium titanate has a typical perovskite structure with cubic packing of Ba^{2+}, O^{2-} ions and Ti^{4+} ions filled the octahedral holes of the crystal (Fig. 2). The ionic radii of Er^{3+}, Yb^{3+} and Zn^{2+} are ~0.89, ~0.86 Å and ~0.75 Å respectively. The Ba^{2+} and Ti^{4+} ions have ionic radii of ~1.61 Å and ~0.605 Å, respectively. The site occupancy of RE ions in perovskite material is well explained on the basis of tolerance factor and thermodynamic considerations by Tsur et al. [29]. According to the study of *Tsur et al*. and *Zulueta et al.*[30], Er^{3+} can occupy both A-sites and B-sites (called amphoteric behaviour) whereas Yb^{3+} ion occupies mainly B-sites because of its enhanced stability at this site in $BaTiO_3$. The ionic radius of Zn^{2+} is very near to that of Ti^{4+}; therefore, Ti-sites are occupied

by Zn, and the overall stoichiometry can be presented through the following stoichiometry relation:

$$(Ba_1)_A(Ti\ Zn_x)_B O_3 \rightarrow (Ba_1)_A(Ti_{1-x}Zn_x^{\cdot})_B(O_{3-x}V_{\ddot{O}}) + xTiO_2$$

where, it is considered that oxygen vacancies are generated only to balance the charge. As a support for this relation, we found the peak for TiO_2 in 20 mol% Zn-doped sample. It is clear from XRD spectra (Fig. 1) that the peak width increases with the Zn addition and a clear peak shift towards higher 2θ value is observed for the 20 mol% Zn-doped sample. Shifting of peak positions toward higher 2θ value reflects a slight expansion of the unit cell volume due to the difference in size of Ti^{4+} ions and Zn^{2+} ions and leads to lattice mismatch.

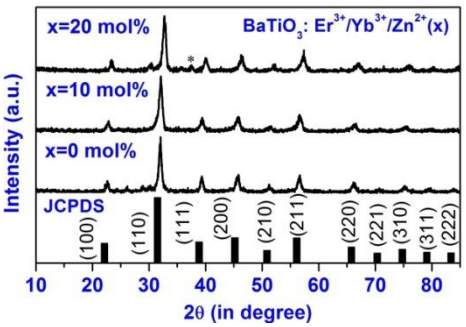

Fig. 1 X-ray diffraction patterns for the 0.3 mol% Er^{3+}, 3.0 mol% Yb^{3+} co-doped $BaTiO_3$ with different amounts of Zn. The pattern shows cubic phase. The samples were annealed at 850 ^{0}C. (* mark corresponds to TiO_2 phase).

The structural parameters, e.g. lattice constant, lattice strain and unit call volume are extracted through XRD analysis [25]. Crystallite size and lattice strain both affect the XRD pattern by peak width and peak position shift. The lattice constant 'a' was calculated according to the h, k, l formula for the cubic system [28]. Comparative studies of lattice parameters of all three samples show that lattice constant increases with increasing Zn^{2+} concentration. This reflects the substitution of Ti^{4+} ions by comparatively larger Zn^{2+} ions.

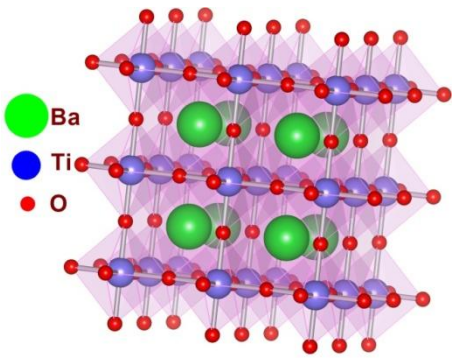

Fig. 2 A 2x2x2 $BaTiO_3$ super cell, with all octahedra. Polyhedra have been drawn to show the coordination of each cation. For pictorial representation Visualization for Electronic and Structural Analysis (VESTA) software [31] was used.

The lattice strain was calculated by using Williamson-Hall equation [28]. Williamson and Hall proposed a method of deconvulating size and strain broadening by looking at the peak width as a function of 2θ and obtained the mathematical formula:

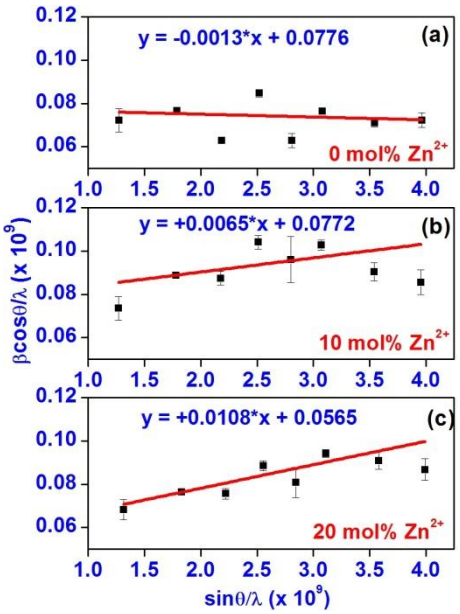

Fig. 3(a-c) W-H analysis of Zn incorporated $BaTiO_3$: Er^{3+}/Yb^{3+} phosphors annealed at 850 ^{0}C. Strain is extracted from slope of the fit.

$$\frac{\beta\cos\theta}{\lambda} = \frac{1}{D} + \frac{\varepsilon\sin\theta}{\lambda} \qquad (1)$$

where, D is the crystallite size, λ is the wavelength of radiation (1.54056 Å for CuK_α), β is the full width at half maximum (FWHM) of the diffraction peak, θ is peak position and ε is the microstrain present in the sample. Plots drawn between sinθ/λ and βcosθ/λ are shown in Fig. 3(a-c). The lattice strains are summarized in Table 1. Figure 3 (a-c) reflects that the slope is changed on Zn-incorporation. The negative slope is because of compressive strain while positive slope indicates the tensile strain [28]. The tensile strain increases with the addition of Zn-content. It indicates that the lattice strain can be tuned towards tensile by adding Zn ions in $BaTiO_3$ lattice. The lattice expansion is thought to increase because of substitution of smaller Ti^{4+} ions by larger Zn^{2+} ions.

Table 1. Lattice constants, lattice strains and lattice volume of all the samples

Sample $BaTiO_3$:Er^{3+}/Yb^{3+}	Lattice constant a (Å)	Lattice strain ε (no unit x 10^{-3})	Unit cell volume V (Å^3)
0 mol% Zn^{2+}	3.967±0.013	-1.3±3.6	62.43
10 mol% Zn^{2+}	3.995±0.018	+6.5±3.4	63.76
20 mol% Zn^{2+}	4.025±0.013	+10.8±2.1	65.21

The increase in strain with Zn addition reflects the increase of resultant distortion because of doping [32].

3.1.2 Fourier Transform Infrared (FTIR) spectroscopy

Fourier transform infrared spectra of three samples annealed at 850^{0}C are shown in Figure 4. All samples exhibit a broad band around 3400 cm^{-1}. This band is assigned to the O-H stretching vibrations of adsorbed water molecules present in the sample. At 2933 cm^{-1} the band is assigned to the C-H stretching vibration. Its intensity does not change and may occur from the environment. The band at 2350 cm^{-1} is assigned to the asymmetric stretching mode of CO_2 [33]. Its intensity increases on Zn addition and is supposed that the Zn modified samples also adsorb CO_2 from the environment. The bands at 1424 cm^{-1} and 856 cm^{-1} are the characteristics for symmetric and bending vibrations of COO^- groups, respectively, arising from residual acetic acid. The intense bands at 653 and 554 cm^{-1} are due to lattice modes of $BaTiO_3$. It is to be noted that the absorption bands due to the organic impurities were found to increase on Zn^{2+} addition. However, the effect of organic contamination on luminescence intensity is not observed.

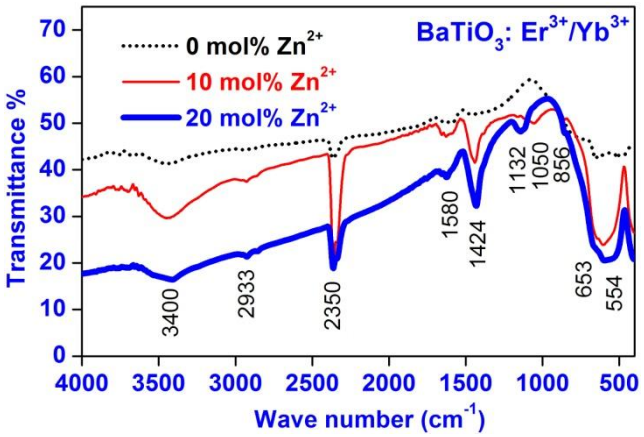

Fig. 4 A comparison in Fourier transform IR spectra of 0, 10 and 20 mol% Zn doped $BaTiO^3$: Er^{3+}/Yb^{3+}.

3.1.3 Microstructure analysis

The scanning electron micrographs (SEM) of three specimens are shown in Figure 5(a-c). As shown in the figure, the shape of the particles is not much affected by the addition of Zn^{2+}. The Zn-doped samples show higher proportion of fine grains while the Zn free sample exhibit larger grains together with small percentage of fine grains. The bright field TEM micrograph of the three samples is shown in Fig 5(d-f) with their selected area electron diffraction (SAED) patterns in the inset. The images reveal the particle size within 40-60 nm in all three samples. The particles are appearing to be connected through grain boundaries. The coherently scattering domains are the crystallite regions of a material and a grain contains multiple domains but in case of nanosized powder the domain size and the particle size are almost equal.

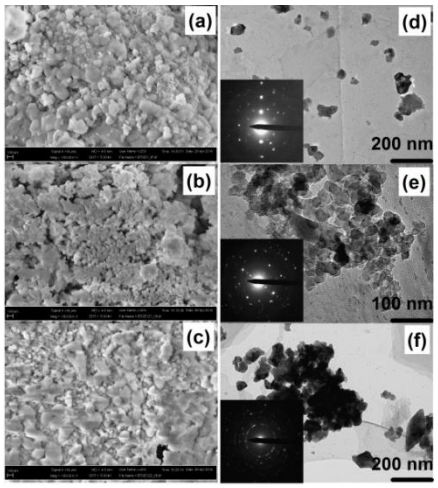

Fig. 5 (a-c) SEM images (d-f) TEM images of 0, 10 and 20 mol% Zn doped $BaTiO_3$: Er^{3+}/Yb^{3+} particles respectively. Inset of (d-f) show the SAED patterns.

3.2 Optical properties

3.2.1 Diffuse reflectance study

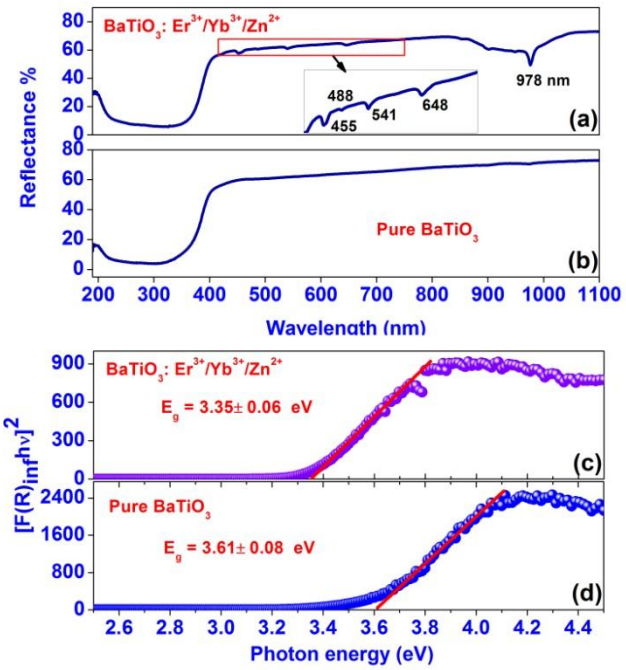

Fig. 6 Diffuse reflectance spectra of (a) $BaTiO_3$:$Er^{3+}/Yb^{3+}/Zn^{2+}$ and (b) pure $BaTiO_3$ phosphor, both annealed at 850 ^{0}C; (c) and (d) are Kubelka-Munk fit to determine optical bandgaps.

The diffuse reflectance spectra of pure and Zn^{2+}-doped barium titanate samples were measured against a reference standard $BaSO_4$ compound. In the diffuse reflectance spectrum (Fig. 6a), the bands are observed at 455, 488, 541, 648 and 978 nm. The strong band around 350 nm is due to the band absorption of barium titanate. The bands located at 455, 488, 541 and 648 nm are due to the transition from ground state $^4I_{15/2}$ to the excited $^4F_{5/2}$, $^4F_{7/2}$, $^2H_{11/2}$ and $^4F_{9/2}$ states, respectively of Er^{3+} ions. The absorption band around 978 nm is due to the transition of Yb^{3+} ions from ground $^2F_{7/2}$ to the excited $^2F_{5/2}$ state.

The bandgaps are estimated by assuming as direct type and calculated using the Kubelka-Munk function and Tauc relation [34]. The bandgap of barium titanate, as an example, was calculated theoretically and experimentally by *Wemple* and *Supasai et al*. [35, 36] respectively. For the band gap calculation we have plotted, $F(R_\infty)h\nu$ against $h\nu$. The K-M function ($F(R_\infty)$) was calculated from the relation, $F(R_\infty)=K/S=(1-R_\infty)/2R_\infty$; where, K and S are the absorption and scattering coefficients and R_∞ is the ratio of reflectance of the sample to that of an ideal non-absorbing standard sample (in our case $BaSO_4$). The band gap (E_g) is related to absorption coefficients using K-M function and Tauc relation for direct type bandgap [34]

$$[F(R_\alpha)h\upsilon] = C_1(h\upsilon - E_g)^m \qquad (2)$$

where, $F(R_\infty)$ is Kubelka-Munk function, $h\nu$ corresponds to the energy of photon, C_1 is a proportionality constant; m= ½ and 2 for direct and indirect type bandgaps respectively. By plotting $[F(R_\infty)h\nu]^{1/m}$ against $h\nu$, the best straight line fitting was obtained for m= ½ (direct type bandgap). The Kubelka-Munk fittings are shown in Fig. 6(c, d) for direct type. The value E_g is obtained by the intersection between linear fit and photon energy axis. The linear portion of the curve characterizes the fundamental absorption and non-linear portion corresponds to a residual absorption involving the impurity states. It is observed that addition of Zn^{2+} in $BaTiO_3$ decreases the optical band gap from 3.61 eV to 3.35 eV. This behaviour is explained on the basis of average bond energy of the system. The presence of Zn^{2+} ions at Ti^{4+} sites lead to the formation of $BaTi_{1-x}Zn_xO_{3-x}$ and acceptor levels which trap the unlocalised electrons thereby creating $Zn_{Ti}^{''}$ acceptor centres that compensate for the V_O defect formed. This substitution leads to change in the compositional and structural properties, because of difference in charge, difference in radii and modification of Ti-O bond length by Zn-O bond length. As the bond energy of Zn-O bond (256 kJ/mol) is lower than that of Ti-O (450.6 kJ/mol) the average bond energy of the system decreases. Since the optical band gap is a bond sensitive property, a decrease in average bond energy of the system results in the reduction of the optical band gap [37].

3.2.2 Upconversion emission study

In the NIR region there are two favourable excitation wavelengths (980 nm and 800 nm) through which Er^{3+}/Yb^{3+} system can efficiently be excited to get UC emission in blue to red regions. The UC emission spectra of $BaTiO_3$: Er^{3+}/Yb^{3+} and $BaTiO_3$: $Er^{3+}/Yb^{3+}/Zn^{2+}$ phosphors, excited by 980 and 800 nm are shown in Fig. 7 (a, b). It should be noted that Fig. 7(a) and 7(b) are recorded at different temperatures. Fig. 7(a) is taken at room temperature (300K) under 980 nm laser excitation while the Fig. 7(b) is taken at 12K under 800nm laser excitation. Due to thermal coupling of $^2H_{11/2}$ and $^4S_{3/2}$ levels, the population of these levels varies with temperature and leads to the variation in their intensities. Moreover, Zn^{2+} doping enhances red emission more due to defects creation in the sample. These spectra show strong emission at 524, 550 and 661 nm and a weak emission at 411 nm. It is observed that under 980 nm excitation the intensities of green and red emission bands are increased by almost 2 and 5 times, respectively, due to addition of 20 mol% Zn^{2+}. Under 800 nm excitation at 12K temperature, an enhancement around 12 and 2 times is found for green and red emission bands (Fig. 7b). Authors have not tried to add higher concentration of zinc because that would likely to degrade other important properties of $BaTiO_3$ such as ferroelectricity, second harmonic generation (SHG) etc. [13]. Substitution of Ti^{4+} ions (ionic radius 0.605 Å) by Zn^{2+} ions (ionic radius 0.750 Å) induces an expansion in the host lattice. The significant enhancement in UC emission intensity is supposed due to the change of local electric field around Er^{3+} ions on doping. Due to this substitution, the symmetry of the local field around the Er^{3+} ions is modified [38]. Under 980 nm excitation the red to green ratio increases

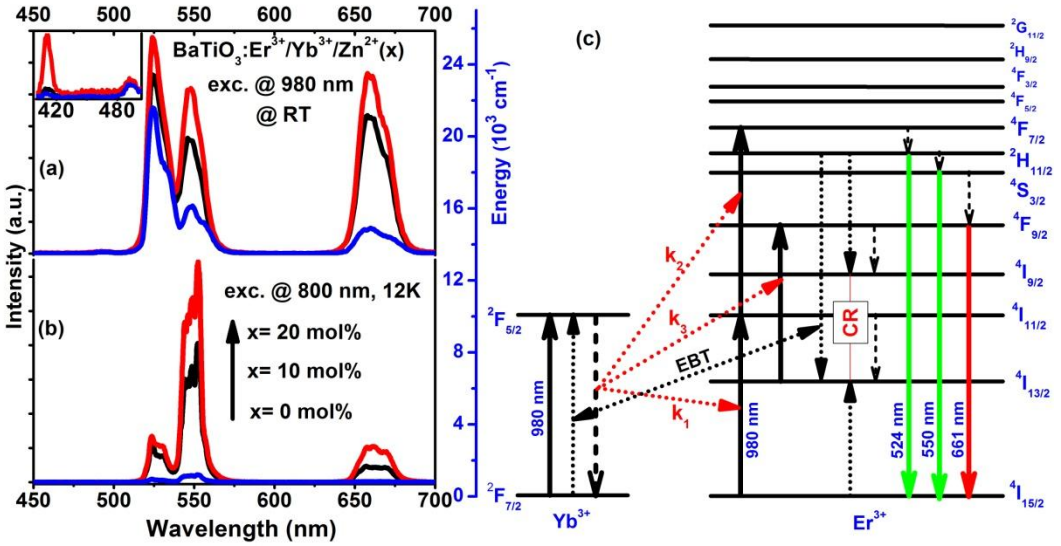

Fig. 7 Examples of UC emission spectra of $BaTiO_3$: Er^{3+}/Yb^{3+} and $BaTiO_3$: $Er^{3+}/Yb^{3+}/Zn^{2+}$ phosphors annealed at 850 ^{0}C (a) excited by 980 nm at room temperature (295K) (b) excited by 800 nm at 12K (c) the energy level diagram with possible pathways.

significantly on Zn^{2+} introduction which consecutively indicates the cross-relaxation (CR) population of the $^4I_{13/2}$ level of Er^{3+} ion.

The UC emission mechanisms can be explained by considering processes such as ground state absorption (GSA), excited state absorption (ESA), cross-relaxation etc. The mechanism of UC using 980 nm is explained well by several workers [8, 18]. Details can be found in our earlier work [28]. Here schematic representation is given in Fig. 7(c).

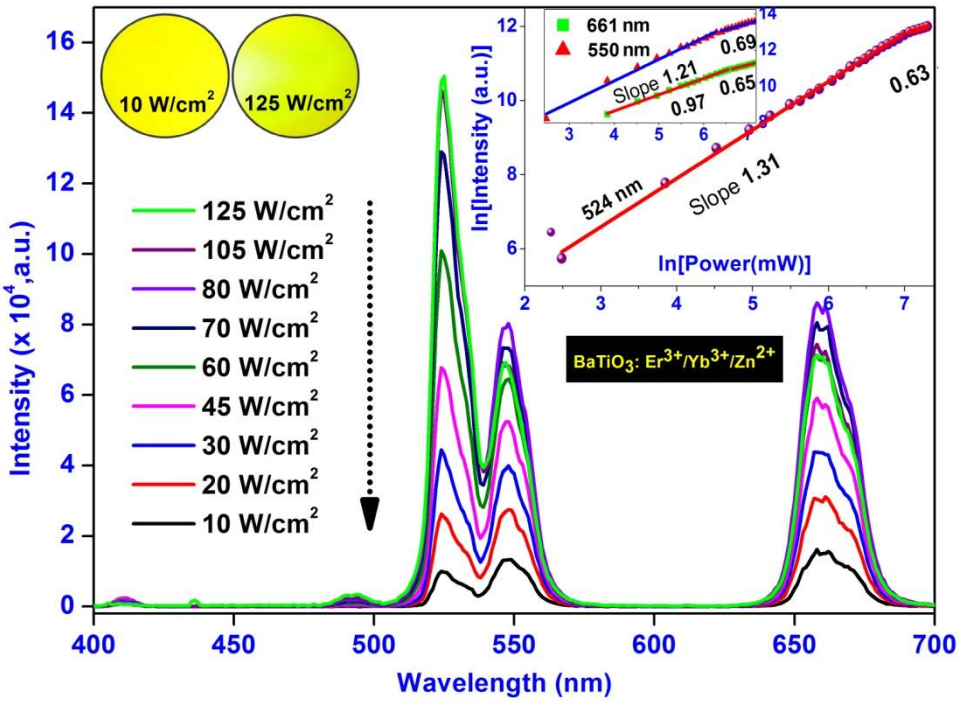

Fig. 8 Variation of UC emission intensity with different input excitation powers of $BaTiO_3$:Er^{3+}/Yb^{3+}/Zn^{2+} (x= 20 mol%). Inset in the right side shows the ln(I)-ln(P) plot of 524, 550 and 661 nm emission bands of $BaTiO_3$:Er^{3+}/Yb^{3+}/Zn^{2+}. The photographs of the sample, shown in left inset were taken at lowest and highest pump power using 980 nm laser.

It is necessary to discuss the large enhancement in red UC emission compared to the green UC emission upon 980nm light excitation. The $^4F_{9/2}$ state is populated via non-radiative decay from the $^4S_{3/2}$ state with the emission of phonons to bridge the energy gap between $^4S_{3/2}$ and $^4F_{9/2}$ states which is ~2800 cm^{-1}. From the FTIR spectra we observed that there is little increase in organic impurities on Zn-doping. Presence of organic impurities is supposed to increase the multiphonon relaxation of $^4S_{3/2}$ level to the $^4F_{9/2}$ level. This multiphonon relaxation then may decrease the intensity of $^4S_{3/2}$ level but it is not visible since change in local field on Zn doping increases the total emission intensity of Er^{3+} ions. There are some other effective channels which are populating the $^4F_{9/2}$ level except the multiphonon relaxation from the upper lying states. The cross-relaxation process, $^2H_{11/2}$/$^4S_{3/2}$ + $^4I_{15/2}$ → $^4I_{9/2}$ + $^4I_{13/2}$, increases the population of the $^4I_{13/2}$ level which eventually leads to populate the $^4F_{9/2}$ level.

The UC emission spectra upon 800 nm excitation are shown in Fig. 7(b). The emission bands are observed at same positions as that with 980 nm excitation because similar transitions involved. Here Yb^{3+} ions has little role in upconversion emission. In this case, Er^{3+} ions in the ground state ($^4I_{11/2}$) absorb 800 nm photon and are excited to the $^4I_{9/2}$ level. The lower $^4I_{11/2}$ and $^4I_{13/2}$ levels are populated via decay of $^4I_{9/2}$ level. These lower lying excited levels have longer lifetimes and hence these levels are populated sufficiently. The ions in these levels may again absorb another 800 nm photon via excited state absorption process and get excited to higher $^4F_{3/2}$ and $^4S_{3/2}$($^2H_{11/2}$) levels. The $^2H_{11/2}$ → $^4I_{15/2}$ and $^4S_{3/2}$ → $^4I_{15/2}$ transitions give rise to two emission bands located at 524 and 550 nm. The remaining population of Er^{3+} ions in the $^2H_{11/2}$ and $^4S_{3/2}$ levels relax non-radiatively to $^4F_{9/2}$ level and finally the $^4F_{9/2}$ → $^4I_{15/2}$ transition gives rise to the red emission around 661 nm.

(a) Influence of input excitation power on upconversion dynamics

In order to understand the upconversion mechanisms, the UC emission intensity was measured at different laser excitation pump-powers (980 nm excitation). As a non-linear effect, the input power dependence of the UC luminescence intensity I(P) is described as $I(P) \propto P^n$, where n is the number of IR photons that must be absorbed for the emission of one upconversion photon and P is the input laser power [39]. Thus, the plot of ln[I(P)] vs. ln[P] reveals the nature of the upconversion i.e. the number of photons absorbed in the upconversion process. Figure 8 compares the emission spectra at different excitation power densities for $BaTiO_3$: Er^{3+}/Yb^{3+}/Zn^{2+} phosphor.

From the figure it is evident that the intensity of all the bands increases as expected but the rate of increase of 525 nm emission band is faster than the band at 550 nm. Moreover, rate of increase of green emission intensity (525-550 nm) is faster than that of red (661 nm) emission band and because of this relative variation in intensity, emission color of the sample shifts from yellow to greenish (inset of Fig. 8). For both $BaTiO_3$: Er^{3+}/Yb^{3+}/Zn^{2+} and

$BaTiO_3$: Er^{3+}/Yb^{3+} samples the values of 'n' for all the bands decrease at higher pump powers (inset, Fig. 8). The values of 'n' for two pump power regions are presented in Table 2. According to the energy level diagram (Fig. 7c), all three transitions should be through two photon absorption process (n ~ 2.0). Among the three slope values, two values viz. 1.31 and 1.21 supports two photon process but the value 0.97 for $^4F_{9/2} \rightarrow {}^4I_{15/2}$ transition falls below the two photon absorption process. It can be explained by considering the cross-relaxation of $^4F_{9/2}$ level. Two ions in this level share their energy in such a way that one goes to $^4S_{3/2}$ and other goes to $^4I_{9/2}$ level. A part of energy of $^4F_{9/2}$ level is transferred back to the $^4S_{3/2}$ level and a decrease in slope value occurs. Moreover, at higher pump powers the slope values decrease due to the saturation effect. In this case a part of excitation energy is lost in the form of heat. The saturation of intensity at higher pump power is studied theoretically in the next section.

Table 2: Slopes of lnP vs. lnI plots

Emission bands	$BaTiO_3$: $Er^{3+}/Yb^{3+}/Zn^{2+}$		$BaTiO_3$: Er^{3+}/Yb^{3+}	
	moderate power	high power	moderate power	high power
524 nm	1.31±0.02	0.63±0.02	1.81±0.02	0.82±0.02
550 nm	1.21±0.02	0.69±0.02	1.23±0.03	0.69±0.02
661 nm	0.97±0.02	0.65±0.02	1.11±0.02	0.67±0.04

(b) Theoretical description of pump-power dependent upconversion dynamics

The concentration ratio of Er^{3+} to Yb^{3+} in the synthesized material is 1:10. Therefore, it is much reasonable to consider the energy transfer from Yb^{3+} to Er^{3+} due to the much larger absorption cross-section (~7 times) of Yb^{3+} compared to Er^{3+} at 980 nm excitation wavelength [40]. The three energy transfer upconversion (ETU) processes from Yb^{3+} to Er^{3+} are (refer to Fig. 7c)-

(a) ETU-1: $^2F_{5/2}$ (Yb^{3+}) + $^4I_{15/2}$ (Er^{3+}) → $^2F_{7/2}$ (Yb^{3+}) + $^4I_{11/2}$ (Er^{3+})

(b) ETU-2: $^2F_{5/2}$ (Yb^{3+}) + $^4I_{11/2}$ (Er^{3+}) → $^2F_{7/2}$ (Yb^{3+}) + $^4F_{7/2}$ (Er^{3+})

(c) ETU-3: $^2F_{5/2}$ (Yb^{3+}) + $^4I_{13/2}$ (Er^{3+}) → $^2F_{7/2}$ (Yb^{3+}) + $^4F_{9/2}$ (Er^{3+})

The Er^{3+} ions raised to the $^4F_{7/2}$ level by ETU-2, relaxes non-radiatively to $^2H_{11/2}/^4S_{3/2}$ levels and subsequently, radiative transition to ground state ($^4I_{15/2}$) yields 525 nm/550 nm emission bands. Possible mechanisms for population of the $^4I_{13/2}$ level of Er^{3+} are (i) energy back-transfer: $^2H_{11/2}/^4S_{3/2}$ (Er^{3+}) + $^2F_{7/2}$ (Yb^{3+}) → $^4I_{13/2}$ (Er^{3+}) + $^2F_{5/2}$ (Yb^{3+}) and (ii) cross-relaxation process of Er^{3+} ions: $^2H_{11/2}/^4S_{3/2}$ + $^4I_{15/2}$ → $^4I_{9/2}$ + $^4I_{13/2}$.

For better understanding of power dependent anomalous behaviour, a theoretical description has been utilized based on the steady-state rate equations for Er^{3+} and Yb^{3+} co-doped system:

$$\frac{dE_{Er,1}}{dt} = 0 = W_2 N_{Er,2} + W' N_{Er,4} N_{Yb,0} + C_{40} N_{Er,4} N_{Er,0} - k_3 N_{Er,1} N_{Yb,1} - W_1 N_{Er,1} - \rho_P \sigma_{13} N_{Er,1} \quad (3)$$

$$\frac{dN_{Er,2}}{dt} = 0 = k_1 N_{Er,0} N_{Yb,1} + \rho_P \sigma_{02} N_{Er,0} - k_2 N_{Er,2} N_{Yb,1} - W_2 N_{Er,2} - \rho_P \sigma_{24} N_{Er,2} \quad (4)$$

$$\frac{dN_{Er,3}}{dt} = 0 = k_3 N_{Er,1} N_{Yb,1} + \rho_P \sigma_{13} N_{Er,1} - W_4 N_{Er,4} - W_3' N_{Er,3} \quad (5)$$

$$\frac{dN_{Er,4}}{dt} = 0 = k_2 N_{Er,2} N_{Yb,1} + \rho_P \sigma_{24} N_{Er,2} - W_4 N_{Er,4} - W_4' N_{Er,4} - W' N_{Er,4} N_{Yb,0} - C_{40} N_{Er,4} N_{Er,0} \quad (6)$$

$$\frac{dN_{Yb,1}}{dt} = 0 = \rho_P \sigma_{Yb} N_{Yb,0} + W' N_{Er,4} N_{Yb,0} - (k_1 N_{Er,0} + k_2 N_{Er,2} + k_3 N_{Er,1}) N_{Yb,1} - W_{Yb} N_{Yb,1} \quad (7)$$

Where, $N_{Er,\,i}$ (i=0, 1, 2, 3, 4) are the population densities of $^4I_{15/2}$, $^4I_{13/2}$, $^4I_{11/2}$, $^4F_{9/2}$ and $^2H_{11/2}/^4S_{3/2}$ levels respectively of Er^{3+}. $N_{Yb,\,i}$ (i=0, 1) are the population densities of $^2F_{7/2}$ and $^2F_{5/2}$ levels respectively of Yb^{3+}. W_1, W_2, W_4 are the non-radiative decay rates of $^4I_{13/2}$, $^4I_{11/2}$ and $^2H_{11/2}/^4S_{3/2}$ states respectively; W'_3, W'_4 are the radiative decay rates of $^4F_{9/2}$ and $^2H_{11/2}/^4S_{3/2}$ states respectively. W_{Yb} is the radiative decay rate of excited state $^2F_{5/2}$ of the Yb^{3+} ion. k_1, k_2 and k_3 are the energy transfer rates of ETU-1, ETU-2 and ETU-3 respectively. C_{40} is the cross-relaxation rate for $^2H_{11/2}/^4S_{3/2}$ + $^4I_{15/2}$ → $^4I_{9/2}$ + $^4I_{13/2}$; W' is the energy back-transfer rate to the Yb^{3+} ions; σ_{ij} is the absorption cross-section between level i and j of Er^{3+}; σ_{Yb} is the absorption cross-section between level $^2F_{5/2}$ and $^2F_{7/2}$ of Yb^{3+}; ρ_P is the pump constant which is proportional to the incident pump power, I_P [41]. Due to low absorption cross-section of Er^{3+} compared to that of Yb^{3+} at 980 nm, the GSA and ESA processes of Er^{3+} states are negligible with comparison to the energy transfer upconversion (by Yb^{3+}). Therefore we can exclude the corresponding GSA and ESA terms from the rate equations. We can ignore the depopulation term of $^2H_{11/2}/^4S_{3/2}$ level associated with the cross-relaxation process because the other radiative and non-radiative relaxation processes are much more dominating depopulation mechanism for this coupled level.

At low pump power, we assume that the spontaneous decays of $^4I_{11/2}$ and $^4I_{13/2}$ levels are dominating de-population mechanisms over ETU-2 and ETU-3. In such a situation we can neglect the corresponding ETU terms in equations (3) and (4). Also, in comparison to direct absorption of 980 nm excitation from $^2F_{7/2}$ to $^2F_{5/2}$ (Yb^{3+}), we can neglect the contribution of energy back-transfer in populating the $^2F_{5/2}$ state. Therefore, equation (7) reduces to

$$N_{Yb,1} = \frac{\rho_P \sigma_{Yb} N_{Yb,0}}{(W_{Yb} + k_1 N_{Er,0} + k_2 N_{Er,2} + k_3 N_{Er,1})} \propto I_P \quad (8)$$

From equations (4) and (5), we obtain

$$N_{Er,1} = \frac{W_2}{W_1} N_{Er,2} + \frac{W'}{W_1} N_{Er,4} N_{Yb,0} + \frac{C_{40}}{W_1} N_{Er,4} N_{Er,0} \quad (9)$$

$$N_{Er,2} = \frac{k_1}{W_2} N_{Er,0} N_{Yb,1} \quad (10)$$

Using equations (10) and (9) in equations (6) and (5), we get

$$N_{Er,4} = \frac{k_2}{(W_4 + W_4^{'} + W^{'} N_{Yb,0})} N_{Er,2} N_{Yb,1} \quad (11)$$

$$N_{Er,3} = \frac{k_3 W_2}{W_1 W_3^{'}} N_{Er,2} N_{Yb,1} + \frac{k_3 (W^{'} + C_{40})}{W_1 W_3^{'}} N_{Er,4} N_{Yb,1} N_{Yb,0} + \frac{W_4}{W_3^{'}} N_{Er,4} \quad (12)$$

Equation (11) indicates that the green emission ($^2H_{11/2}/^4S_{3/2}$) has a quadratic dependence on pump power involving ETU-1 +ETU-2 + non-radiative relaxation to $^2H_{11/2}/^4S_{3/2}$ process whereas eq. (12) shows that the red emission is quadratic as well as cubic power dependent process (x I_P^2+y I_P^3+z I_P^2). The quadratic power dependent term (1st term of eq. 12) is due to the upconversion preceded by ETU-1 + ETU-2 + non-radiative relaxation to $^4F_{9/2}$ process while the three photon upconversion (2nd term of eq. 12) is associated with the ETU-1 + ETU-2 + non-radiative relaxation to $^2H_{11/2}/^4S_{3/2}$ + (EBT + CR) + ETU-3 process. If the contributions of energy back-transfer and cross-relaxation processes are neglected in eq. (12), we get exactly the two-photon dependency of red upconversion. At low pump power, the red emission contains the cubic and quadratic power dependent terms but our experimental data (Fig. 8) shows only quadratic power dependency which indicates that the theoretical model is ideal at very low power and our obtained result is in intermediate state when pump power density increases towards higher value. So, a competition between the decay rates and ETU's is already started by that time.

At high pump power, we will assume that the energy transfer upconversions- ETU-2 and ETU-3 are dominant over linear decays of the $^4I_{11/2}$ and $^4I_{13/2}$ states. Therefore, we will ignore the terms- $W_1N_{Er,1}$ and $W_2N_{Er,2}$ in eqs. (3) and (4) respectively. Eqs. (3) and (4) reduces to

$$N_{Er,1} = \frac{W_2}{k_3 N_{Yb,1}} N_{Er,2} + \frac{W^{'}}{k_3 N_{Yb,1}} N_{Er,4} N_{Yb,0} + \frac{C_{40}}{k_3 N_{Yb,1}} N_{Er,4} N_{Er,0} \quad (13)$$

$$N_{Er,2} = \frac{k_1}{k_2} N_{Er,0} \propto I_P^0 \quad (14)$$

and consequently we get,

$$N_{Er,4} = \frac{k_2}{(W_4 + W_4^{'} + W^{'} N_{Yb,0})} N_{Er,2} N_{Yb,1} \quad (15)$$

$$N_{Er,3} = \frac{W_2}{W_3^{'}} N_{Er,2} + (\frac{W^{'}}{W_3^{'}} N_{Yb,0} + \frac{C_{40}}{W_3^{'}} N_{Er,0}) N_{Er,4} + \frac{W_4}{W_3^{'}} N_{Er,4} \quad (16)$$

Equation (15) shows that the green emission becomes a single photon absorption process. Eq. (16) is proportional to (xI_P^0+yI_P^1+zI_P^1). It is to be noted that the first term in eq. (16) is associated with the ETU-1 + ETU-2 + non-radiative relaxation to $^4F_{9/2}$ state; the third term is involved with the- ETU-1 + non-radiative decay to $^4I_{13/2}$ + ETU-3 process and the second term is the process related to the process ETU-1 +ETU-2 + non-radiative relaxation to $^2H_{11/2}/^4S_{3/2}$ + (EBT+CR) + ETU-3. As the pump power increases from low to high density, the population of the $^4F_{9/2}$ state becomes independent of the pump power, which means that the ETU-2 process becomes highly efficient at high power density and the green emission also reduces from I_P^2 to I_P. The energy back-transfer and cross-relaxation processes become much more efficient at high pump power to saturate the $^4I_{13/2}$ level and the power dependence of red emitting level $^4F_{9/2}$ decreases from I_P^3 & I_P^2 to I_P. This consideration agrees well with the experimental data presented in Fig. 8 and explains the abnormal power dependent behaviour, listed in Table 2.

(c) Site-selective time-resolved spectroscopy

To get an idea on the nature of rare earth ion occupancy and role of Zn ions in $BaTiO_3$ lattice, the lifetime studies were conducted by excitation with 800 nm laser light. The decay curves corresponding to the $^4S_{3/2}$ and $^4F_{9/2}$ levels of Er^{3+} ions in the 0.3 mol% erbium – 3mol% ytterbium doped barium titanate with different concentrations of zinc are shown in Fig. 9. The decay lifetime measurements of $^4S_{3/2}$ and $^4F_{9/2}$ levels (Er^{3+}) for all the samples ($BaTiO_3$: Er^{3+}/Yb^{3+} and $BaTiO_3$: $Er^{3+}/Yb^{3+}/Zn^{2+}$) have been performed at low temperature (12K) and are presented in Table 3. The decay times of $^4S_{3/2}$ and $^4F_{9/2}$ levels were best fitted by a double-exponential function [42]

$$I(t) = I_0 + A_1 e^{-t/\tau_1} + A_2 e^{-t/\tau_2} \quad (17)$$

Where, I(t) and I_0 denotes the luminescence intensities at time t and 0 respectively. A_1 and A_2 are fitting parameters and τ_1, τ_2 are the short and long components of the luminescence decay times. The occupancy percentage of Er^{3+} ions showing a specific decay time is obtained using the following formula [43],

$$\% \text{ of species} = \frac{A_i \tau_i}{\sum_{i=1,2} A_i \tau_i} \times 100 \quad (18)$$

Analysis shows the presence of two components, one short-lived and another long lived, which indicates the presence of two emitting species. In a cubic $BaTiO_3$, the Ba^{2+} ions are located at the eight corners of the unit cell, Ti^{4+} ions are located at the centre of the unit cell, O^{2-} ions are at the centre of the cubic faces (Fig. 2); The Er^{3+} ions in $BaTiO_3$ lattice most probably occupy the Ba-site. The second possibility may be at Ti-site (amphoteric nature). As the Er^{3+} ions have two different co-ordination at two sites (A-site and B-site), the decay time also changes according to their site-occupancy.

For a given host lattice (fixed phonon energy), a relatively shorter decay time, should be attributed to an asymmetric or less symmetric site, due to relaxation in the selection rules, whereas a longer decay time is often associated with a more symmetric site due to the difficulties in f-f transitions [43]. In the present scenario, the shorter decay time is assumed to arise because of the 6-coordinated Er^{3+} ion in the Ti-site, whereas the longer decay time is associated with Er^{3+} ions occupying the 12-coordinated Ba-site. The occupancy of Er^{3+} ions at Ba-site exhibiting long decay time is obtained as 82% while it is found to be 18% at Ti-site with shorter decay time. The site-selective spectroscopy of trivalent samarium ions in perovskite $SrZrO_3$ was studied by *Gupta et al.* [43] and found A-site occupancy as the minor species and a B-site occupancy as the major species for samarium ions, which is just reverse of our result of occupying Er^{3+} ions in A-site and B-site of $BaTiO_3$ lattice.

The luminescence of Sm^{3+} in the $BaTiO_3$ host lattice was previously investigated by *Makishim et al.* [44] and it was observed that the spectra consist of two different group of

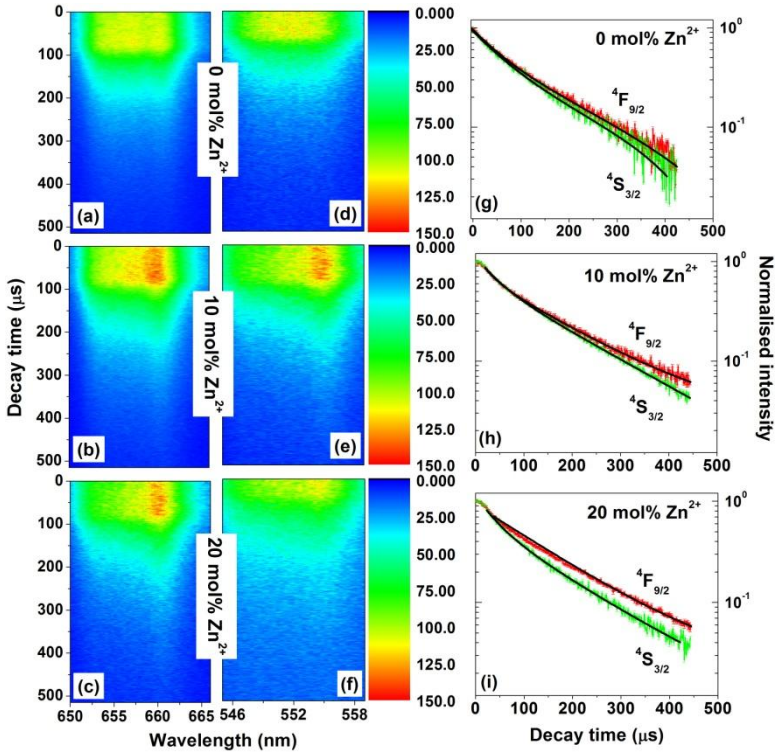

Fig. 9 (a-c & d-f) Time-resolved survey spectra recorded at 12K for $^4F_{9/2}$ and $^4S_{3/2}$ states respectively of Er^{3+} of 0 mol%, 10 mol% and 20 mol% Zn^{2+} doped in $BaTiO_3$: Er^{3+}/Yb^{3+}; (g-i) time-resolved luminescence decay curves of $^4F_{9/2}$ and $^4S_{3/2}$ states of Er^{3+} in $BaTiO_3$: Er^{3+}/Yb^{3+} and $BaTiO_3$: $Er^{3+}/Yb^{3+}/Zn^{2+}$ at 12K.

spectral lines. They also mentioned that certain foreign ions can change the relative strength of emissions in the two series due to a charge compensation mechanism. Based on their results, it was concluded that one group of spectral lines is attributed to Sm^{3+} at the Ti^{4+} site, while the other group of spectral lines is related to the presence of Sm^{3+} at the Ba^{2+} site. A similar observation of decay lifetime for Eu^{3+} ions in α-$Zn_2P_2O_5$ was studied, where such kind of short and long components were explained on the basis of site-selective spectroscopy of Eu^{3+} in 6-co-ordinated and 5-co-ordinated Zn-sites respectively [45].

The short and long components for $^4S_{3/2}$ level (550 nm emission) were prolonged by ~11 % and ~35 % respectively after 20 mol% Zn-incorporation. The Zn^{2+} ions enter into the barium titanate host lattice, and some Zn^{2+} ions occupy interstitial sites while others substitute Ti^{4+}. This phenomenon can tailor the local crystal field around the RE^{3+} and causes the prolongation of the decay lifetimes of the red and green emitting bands ($^4F_{9/2}$, $^4S_{3/2}$). The longer decay lifetime with Zn^{2+} ions introduction, indicates that the Zn^{2+} doping improves the luminescence. According to the transition rules for rare earth ions between different energy levels in $4f^n$-configaration: $|\Delta J| = 2$, $|\Delta L| = 0, \pm 1$, $S = 0$, provided that the electric dipole transitions are not allowed between the states with same parity. However, through the Zn^{2+} introduction in barium titanate lattice, the crystal field is changed and inversion symmetry is lost, which may allow to break the transition rules and electric dipole transition probability increases. The enhancement of upconversion luminescence in Er-Yb system in oxide and fluoride matrices have also been studied earlier and observed the prolongation of lifetime of $^4S_{3/2}$ and $^4F_{9/2}$ states of Er^{3+} ions by introducing Li^+ ions in the host lattice [18, 46, 47].

Table 3 Short and long components of decay time of $^4S_{3/2}$ and $^4F_{9/2}$ states

Energy state		$BaTiO_3$: Er^{3+}/Yb^{3+}		
		0 mol% Zn^{2+} (μs)	10 mol% Zn^{2+} (μs)	20 mol% Zn^{2+} (μs)
$^4S_{3/2}$	t_1	25.6±1.2	31.7±1.9	34.6±0.9
	t_2	125±5	133±4	138.±3
$^4F_{9/2}$	t_1	27±3	34±3	37.5±1.5
	t_2	138±6	163±8	164±5

(d) Temperature sensing

The upconversion efficiency is governed by the non-radiative processes and the non-radiative process depends on the energy gap between the associated higher and lower energy levels as well as the phonon energy of the material. With increasing temperature, the emission of phonons increases. The multiphonon non-radiative decay rate can be presented according to the energy gap law as [48].

$$W_{mp}(T) = W_{mp}(0)[1 - e^{-\frac{h\upsilon}{kT}}]^{-n} \quad (19)$$

where $W_{mp}(T)$ and $W_{mp}(0)$ are the nonradiative decay rate at temperatures T and 0K respectively, hν is the relevant phonon energy, n = $\Delta E/h\nu_{max}$ is the minimum number of phonons

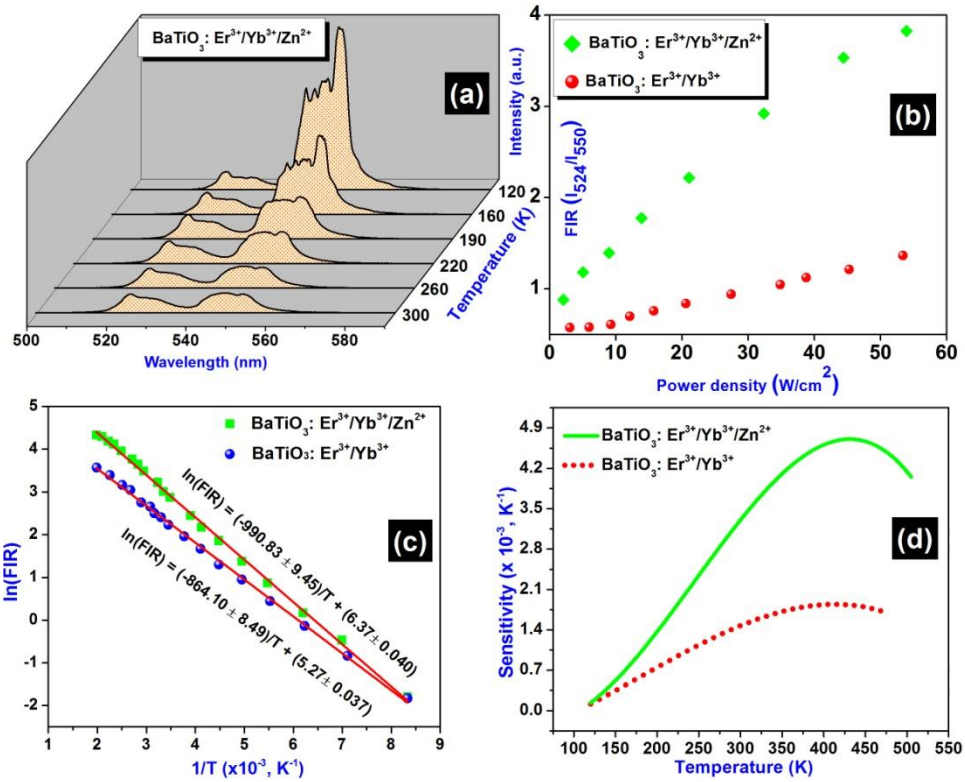

Fig. 10(a) Temperature dependent upconversion of $BaTiO_3$: $Er^{3+}/Yb^{3+}/Zn^{2+}$ excited at 980 nm (b) variation of FIR with input pump power (c) monolog plot of FIR as a function of inverse absolute temperature (d) sensitivity as a function of absolute temperature, of $BaTiO_3$: Er^{3+}/Yb^{3+} and $BaTiO_3$: $Er^{3+}/Yb^{3+}/Zn^{2+}$ samples.

required to bridge the energy gap, ΔE between the relaxing and next lower state and $h\nu_{max}$ is the highest energy of phonon . This equation shows that if the phonon energy of the material is low, the nonradiative relaxations are obstructed and hence the upconversion emission increases. When energy gap between the two relevant levels becomes equal to 3-4 times of the phonon energy, the multiphonon relaxation process is found to be competitive with the radiative process and this competition could be seen in temperature dependent studies.

The intensity ratio of the emission bands cantered at 524 and 550 nm is plotted against excitation power and shown in Figure 10b. This type of variation in intensity ratio can be correlated with the temperature dependent behaviour. It is observed that with increasing pump power, the intensity ratio first increases in a well fashion (~linear). This may happen due to the population saturation of the excited energy levels at high power densities. This type of variation in upconversion emission intensities with excitation power inspired us to study the temperature dependent upconversion emissions.

Temperature sensing behaviour of Er^{3+}/Yb^{3+} co-doped YVO_4 nanophosphor using the luminescence bands cantered at 524 and 554 nm was reported in our previous work [48]. *Vetrone et al.* [3] has demonstrated that $NaYF_4$: Er^{3+}/Yb^{3+} nanoparticles can be used as nanoprobes based on the fluorescence intensity ratio (FIR) of the two thermally coupled bands emitted due to $^2H_{11/2} \rightarrow {}^4I_{15/2}$ and $^4S_{3/2} \rightarrow {}^4I_{15/2}$ transitions of Er^{3+} ion. Temperature dependent upconversion of $BaTiO_3$: $Er^{3+}/Yb^{3+}/Zn^{2+}$ is shown in Fig. 10a. The FIR variation with temperature is plotted in Fig. 10c. Two closely separated energy levels (few k_BT) show Boltzmann type population ratios and the integrated fluorescence intensity ratio (FIR) of transitions $^2H_{11/2} \rightarrow {}^4I_{15/2}$ and $^4S_{3/2} \rightarrow {}^4I_{15/2}$ could be represented as [49]:

$$FIR = \frac{I_{524}(^2H_{11/2} \rightarrow {}^4S_{15/2})}{I_{554}(^4S_{3/2} \rightarrow {}^4I_{15/2})} = \frac{W_H g_H h\upsilon_H}{W_S g_S h\upsilon_S} \exp(-\frac{\Delta E}{k_B T}) = B\exp(-\frac{\Delta E}{k_B T}) \quad (20)$$

where, I_{524} and I_{550} are the integrated intensities corresponding to $^2H_{11/2} \rightarrow {}^4I_{15/2}$ (~524 nm) and $^4S_{3/2} \rightarrow {}^4I_{15/2}$ (~554 nm) transitions of Er^{3+}, W_H and W_S are the radiative probabilities of the two transitions, g_H and g_S are the (2J+1) degeneracies of levels $^2H_{11/2}$ and $^4S_{3/2}$ respectively, and $h\nu_H$ and $h\nu_S$ are the photon energies of the $^2H_{11/2} \rightarrow {}^4I_{15/2}$ and $^4S_{3/2} \rightarrow {}^4I_{15/2}$ transitions respectively, ΔE is the energy gap between the two emitting levels, k_B is the Boltzmann constant and T is absolute temperature. Equation (20) can be expressed as follow:

$$\ln(FIR) = \ln(B) + (-\frac{\Delta E}{k_B T}) = \ln(B) + (-\frac{C}{T}) \quad (21)$$

where, B and C are constants that need to be determined. The energy difference, ΔE changes very little with host materials but a change in host's average phonon frequency plays an important role in FIR. The value of B depends on detection system response, degeneracy- g_H, g_S and spontaneous emission probability- W_H, W_S. The degeneracy value is (2J+1) for most of the host materials. Therefore, spontaneous emission probabilities W_H, W_S are the most sensitive variables.

Furthermore, it is important to know the sensitivity of the material, which is defined as the rate at which the FIR changes

with temperature. The absolute sensor sensitivity can be defined as [50, 51].

$$S = \frac{\partial(FIR)}{\partial T} = FIR \times \frac{\Delta E}{k_B T^2} \quad (22)$$

where, all the terms have been discussed earlier. Sensitivity as a function of temperature is presented in figure 10d. With increasing temperature, the absolute sensitivity of the material first increases, then after a certain temperature it starts decreasing. It is noteworthy that the ratio of transition probabilities from the emitting levels represents an amplification factor to the thermal sensitivity. A similar behaviour of temperature dependent sensitivity was also observed in $LiNbO_3$: Er^{3+}/Yb^{3+} sub-micron particles by *Quintanilla et al.* [52]. The maximum value of sensitivity is observed to be 0.00475 K^{-1} at 430K and 0.00192 K^{-1} at 410K in $BaTiO_3$: $Er^{3+}/Yb^{3+}/Zn^{2+}$ and $BaTiO_3$: Er^{3+}/Yb^{3+} samples respectively. These results show that Zn- incorporated $BaTiO_3$:Er^{3+}/Yb^{3+} phosphor could be exploited for temperature sensing with better sensitivity compared to barium titanate without any zinc.

(e) Photometric characterization

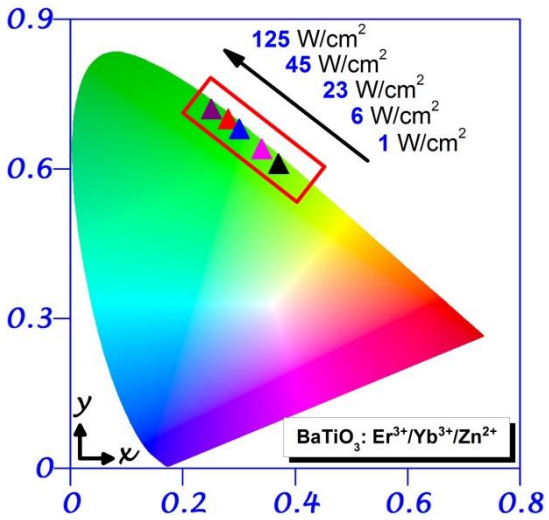

Fig. 11 CIE chromaticity diagram. Variation of emission color on varying excitation power densities for $BaTiO_3$: $Er^{3+}/Yb^{3+}/Zn^{2+}$ phosphor.

The variation of UC emission colour coordinates as a function of input excitation power density is illustrated in the 1931 Commission International l'Eclairage (CIE) chromaticity diagram [53]. The variation of UC emission colour points as a function of input excitation power density is shown in Fig. 11. From the measured spectra, the colour point is significantly changed from yellow to green region with increasing the excitation power. This is because of the increased population of Er^{3+} ions at $^2H_{11/2}$ and $^4S_{3/2}$ states compared to $^4F_{9/2}$ state at high excitation power density. The green to red ratio increases as the excitation power is increased, indicating that green emission is more intense when the sample is excited under higher power. The $^2H_{11/2}/^4S_{3/2}$ and $^4F_{9/2}$ states of Er^{3+} ion are populated by ESA and ETU mechanisms for the green and red upconversion emissions involving two photon processes. The rate constants for the green and red emitting levels are not same and consequently the population processes with pump power are not identical. As a result the population of the $^2H_{11/2}/^4S_{3/2}$ and $^4F_{9/2}$ states show different power dependence and the color is tuned with the laser power. It is expected that the increase in population of $^2H_{11/2}/^4S_{3/2}$ than $^4F_{9/2}$ state is due to the non-equivalent power dependence of the corresponding levels.

3.2.3 Cathodoluminescence study

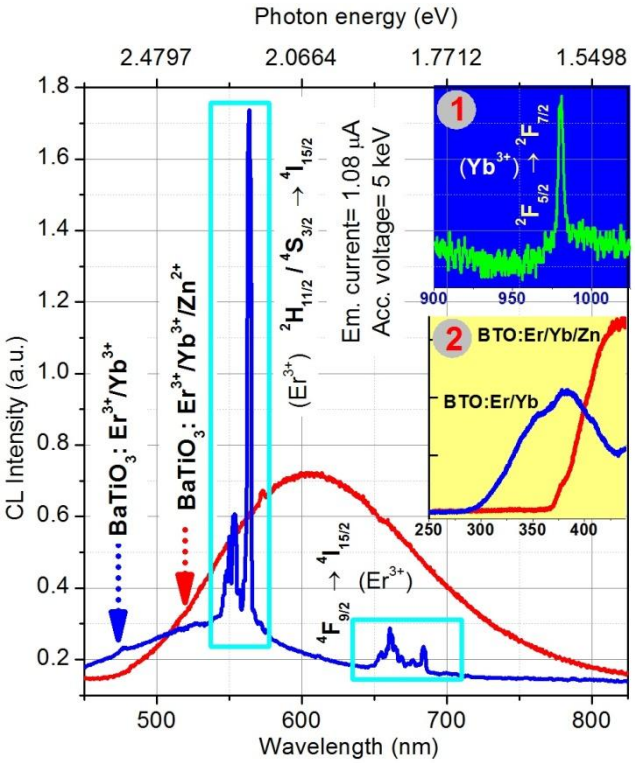

Fig. 12 Cathodoluminescence spectra of $BaTiO_3$: Er^{3+}/Yb^{3+} and $BaTiO_3$: $Er^{3+}/Yb^{3+}/Zn^{2+}$ phosphors; inset 1 shows the emission of Yb^{3+} ions of $BaTiO_3$: Er^{3+}/Yb^{3+} phosphor and inset 2 shows the comparative spectra in the lower wavelength region.

As an additional property of this phosphor, the cathodoluminescence (CL) is reported here in short as field emission displays (FED) application of phosphors [54]. Figure 12 shows a comparison between the CL spectra of $BaTiO_3$: Er^{3+}/Yb^{3+} and $BaTiO_3$: $Er^{3+}/Yb^{3+}/Zn^{2+}$ phosphors under low energy electron beam excitation at 5 keV of accelerating voltage and 1.08 μA of filament current. The $BaTiO_3$: Er^{3+}/Yb^{3+} shows the characteristic emissions for erbium and ytterbium ions (inset 1) having very low defect luminescence while $BaTiO_3$: $Er^{3+}/Yb^{3+}/Zn^{2+}$ shows strong defect luminescence. The inset 2 of Fig. 12 shows the shifting of the luminescence band due to the red shift of optical band gap after Zn-incorporation (section 3.2.1). The luminescence enhancement can be explained in terms of the creation of defects levels due to Zn-doping. The valence and conduction bands of $BaTiO_3$ are dominated by O-2p orbitals and Ti-3d orbitals respectively. As discussed above for time-resolved spectroscopy (section 3.2.2), we have calculated the occupancy of erbium ions in Ba-site and Ti-site as 82% and 18% respectively. The Er^{3+} ions at Ba-site can act as donor and while the Er^{3+} ions at the Ti-site can act as acceptor. With the

incorporation of Zn, the Ti-sites are occupied and acceptor levels are formed which trap the unlocalized electrons and creates $Zn_{Ti}^{''}$ acceptor centres. In order to balance the charge difference, oxygen vacancies are formed and additional energy levels are created by oxygen vacancies within the forbidden energy gap, which contributes to defect luminescence enhancement.

4. Conclusions

Optical functionality is introduced into ferroelectric $BaTiO_3$ via doping of Er^{3+}/Yb^{3+}. The introduction of Zn^{2+} ions in barium titanate lattice has shown enhancement in upconversion and cathodoluminescence emission. Tuning of lattice strain towards tensile is correlated with Ti-site substitution by Zn^{2+} ions. A red shift in the optical bandgap of $BaTiO_3$ on addition of Zn^{2+} ions is observed and explained in terms of bond energy of the system. Time-resolved spectroscopy at low temperature (12K) reveals the presence of Er^{3+} ions at Ba as well as Ti-sites in $BaTiO_3$ lattice. The enhancement in the upconversion emission due to Zn^{2+} introduction may be attributed to the modification of the crystal field symmetry environment around the RE^{3+} ions which alters the emission properties. The temperature dependence of emission, the intensity ratio of two closely spaced emitting levels confirms the potential use of this phosphor as a temperature sensor with maximum sensitivity of $0.00475K^{-1}$ at 430K. This relatively inexpensive ferroelectric material shows potential for multifunctional applications.

Acknowledgements

This project has been funded with support from the European Commission. This publication reflects the views only of the author, and the Commission cannot be held responsible for any use which may be made of the information contained therein. K. Kumar acknowledges Council of Scientific & Industrial Research, New Delhi (no. 03(1303)/13/EMR-II) for financial assistance.

Notes and references

[a]*Second Institute of Physics, University of Goettingen, Friedrich-Hund-Platz 1, 37077 Göttingen, Germany*
[b]*Department of Applied Physics, Indian School of Mines, Dhanbad-826004, India*
[*]*Corresponding author's e-mail address:* mmahata@uni-goettingen.de

1 E. Downing, L. Hesselink, J. Ralston and R. Macfarlane, *Science*, 1996, **276**, 1185.
2 O. S. Wolfbeis, A. Durkop, M. Wu and Z. Lin, *Angew. Chem. Int. Ed.,* 2002, **41**, 4495.
3 F. Vetrone, R. Naccache, A. Zamarron, A. Juarranz de la Fuente, F. Sanz-Rodríguez, L. M. Maestro, E. M. Rodríguez, D. Jaque, J. G. Solé and J. A. Capobianco, *ACS Nano*, 2010, **4**, 3254.
4 D. K. Chatterjee and Y. Zhang, *Nanomedicine*, 2008, **3**, 73.
5 N. Kotov, *Nat. Mater*., 2011, **10**, 903.
6 Z. Gu, L. Yan, G. Tian, S. Li, Z. Chai and Y. Zhao, *Adv. Mater*., 2013, **25**, 3758.
7 F. Wang and X. Liu, *Chem. Soc. Rev.*, 2009, **38**, 976.
8 F. Auzel, *Chem. Rev.,* 2004, **104**, 139.
9 P. Tang, D. J. Towner, A. L. Meier and B. W. Wessels, *Appl. Phys. Lett.*, 2004, **85**, 4615.
10 A. J. Moulson and J. M. Herbert, Electroceramic: Materials, properties, applications, *Chapman and Hall*, 1990, Chap 2, 19 & 72.
11 Y. Ohara, K. Koumoto and H. Yanagida, *J. Am. Ceram. Soc.*, 1985, **68**, C-108.
12 B. Li, S. Zhang, X. Zhou, Z. Chen and S. Wang, *J. Mater. Sci.*, 2007, **42**, 5223.
13 A.Y. Fasasi, M. Maaza, E.G. Rohwer, D. Knoessen, Ch. Theron, A. Leitch and U. Buttner, *Thin Solid Films*, 2008, **516**, 6226.
14 F. A. Rabuffetti, S. P. Culver, J. S. Lee and R. L. Brutchey, *Nanoscale*, 2014, **6**, 2909.
15 H. Hamaji, H. Sano, H. Wada and K. Tomono, in *The 7th US-Japan Seminar on Dielectric and Piezoelectric Ceramics*, edited by T. Yamamoto, 1995, p. 273.
16 J. A. Dawson, C. L. Freeman, J.-B. Ben, J. H. Harding and D. C. Sinclair, *J. Appl. Phys*., 2011, **109**, 084102.
17 Y. Zhang, J. Hao, C. L. Mak and X. Wei, *Opt. Exp.*, 2011, **19**, 1824.
18 Q. Cheng, J. Sui and W. Cai, *Nanoscale*, 2012, **4**, 779.
19 F. Rao, M. Kim, A. J. Freeman, S. Tang and M. Anthony, *Phys. Rev. B*, 1997, **55**, 13953.
20 A. C. Caballero, J.F. Fernández, C. Moure, P. Durán and Y. Chiang, *J. Am. Ceram. Soc.*, 1998, **81**, 939.
21 P. Baxter, N. J. Hellicar and B. Lewis, *J. Am. Ceram. Soc.*, 1959, **42**, 465.
22 M. N. Swillam and A. M. Gadalla, *J. Trans. Br. Ceram.*, 1975, **74**, 165.
23 K. H. Yoon, J. W. Kim and K. H. Jo, *J. Mater. Sci. Lett.*, 1989, **8**, 153.
24 L. H. Fischer, G. S. Harms and O. S. Wolfbeis, *Angew. Chem. Int. Ed.*, 2011, **50**, 4546.
25 K. Mishra, S. K. Singh, A. K. Singh, S. B. Rai, *Mater. Res. Bull.*, 2013, **48**, 4307.
26 C. Joshi, K. Kumar, S. B. Rai, *J. Appl. Phys.*, 2009, **105**, 123103.
27 A. K. Singh, S. Singh, D. Kumar, D. K. Rai, S. B. Rai, K. Kumar, *Opt. Lett.*, 2012, **37**, 776.
28 M. K. Mahata, K. Kumar and V. K. Rai, *Spectrochim. Acta A*, 2014, **124**, 285.
29 Y. Tsur, T. D. Dunbar and C. A. Randall, *J. Electroceram.*, 2001, **7**, 25.
30 Y. A. Zulueta, F. Guerrero, Y. Leyet, J. Anglada-Rivera, R. L. Gonzalez-Romero, J. J. Melendez, *Phys. Status Solidi B*, 2014, **252**, 508.
31 K. Momma and F. Izumi, *J. Appl. Crystallogr.*, 2011, **44,** 1272.
32 M. Zhao, G. Li, J. Zheng, L. Li, H. Wang and L. Yang, *CrystEngComm.*, 2013, **13**, 6251.
33 G. Busca, V. Buscaglia, M. Leoni and P. Nannit, *Chem. Mater.*, 1994, **6**, 955.
34 S. Som and S. K. Sharma, *J. Phys. D: Appl. Phys.*, 2012, **45**, 415102.
35 S. H. Wemple, *Phys. Rev. B*, 1970, **2**, 2679.
36 T. Supasai, S. Dangtip, P. Learngarunsri, N. Boonyopakorn, A. Wisitsoraat, S. K. Hodak, *Appl. Surf. Sci.*, 2010, **256**, 4462.
37 D. R. Lide (Ed.), *CRC Handbook of Chemistry and Physics*, CRC, Boca Raton, FL (2002).
38 L. Yang, L. Li, M. Zhaoa and G. Li, *Phys. Chem. Chem. Phys.*, 2012, **14**, 9956.
39 J. F. Suyver, A. Aebischer, S. García-Revilla, P. Gerner and H. U. Güdel, *Phys. Rev. B*, 2005, **71**, 125123.
40 F. Huang, X. Liu, Y, Ma, S. Kang, L. Hu and D. Chen, *Sci. Rep.*, 2015, **5**, 8233.
41 M. Pollnau, D. R. Gamelin, S. R. Luethi and H. U. Guedel, *Phys. Rev. B*, 2000, **61**, 3337.

42 L. P. Li, M. L. Zhao, W. M. Tong, X. F. Guan, G. S. Li and L. S. Yang, *Nanotechnology*, 2010, **21**, 195601.

43 S. K. Gupta, P. S. Ghosh, N. Pathak, A. Aryab and V. Natarajana, *RSC Adv.*, 2014, **4**, 29202.

44 S. Makishim, H. Yamamoto, T. Tomotsu and S. Shionoya*, J. Phys. Soc. Jpn.*, 1965, **20**, 2147.

45 S. K. Gupta, M. Mohapatra, S. V. Godbole and V. Natarajan, *RSC Adv.*, 2013, **3**, 20046.

46 C. Zhao, X. Kong, X. Liu, L. Tu, F. Wu, Y. Zhang, K. Liu, Q. Zenga and H. Zhang, *Nanoscale*, 2013, **5**, 8084.

47 G. Y. Chen, H. C. Liu, G. Somesfalean, Y. Q. Sheng, H. J. Liang, Z. G. Zhang, Q. Sun and F. P. Wang, *Appl. Phys. Lett.*, **92,** 113114.

48 M. K. Mahata, K. Kumar and V. K. Rai, *Sensor. Actuat. B-Chem.*, 2015, **209**, 775.

49 R. Dey and V. K. Rai, *Dalton Trans.*, 2014, **43**, 111.

50 M. K. Mahata, S. P. Tiwari, S. Mukherjee, K. Kumar and V. K. Rai, *J. Opt. Soc. Am. B*, 2014, **31,** 1814.

51 S. P. Tiwari, M. K. Mahata, K. Kumar, V. K. Rai, *Spectrochim. Acta A*, 2015, **150**, 623.

52 M. Quintanilla, E. Cantelar, F. Cusso, M. Villegas and A. C. Caballero, *Appl. Phys. Express*, 2011, **4**, 022601.

53 "Commission Internationale de l'Eclairage, Huitieme Session, Cambridge, September 1931" *Recueil des Travaux et Compte Rendu des Seances,* The University Press. Cambridge 1932, Resolution 2. pp**.** 19-23.

54 G. Li and J. Lin, *Chem. Soc. Rev.*, 2014, **43**, 7099.